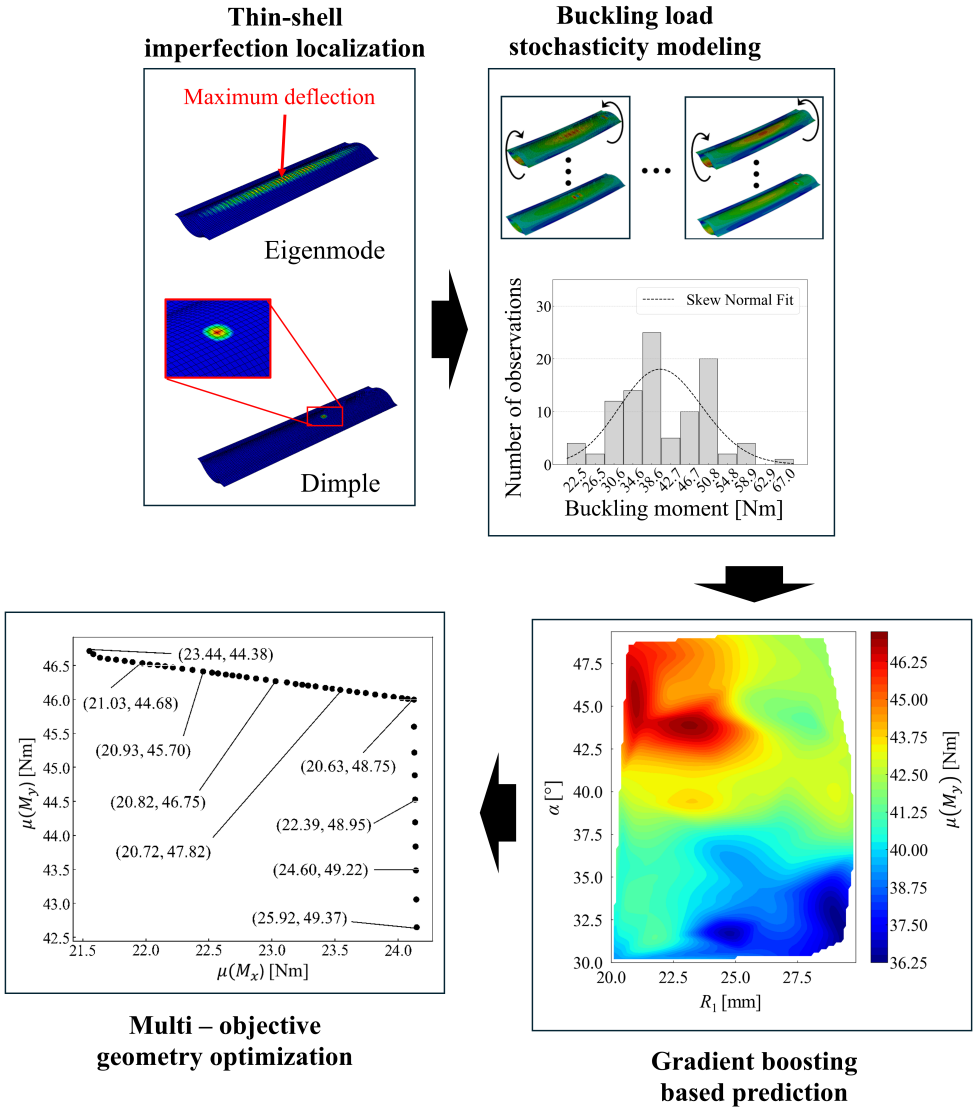
Graphical Abstract

A Data-Driven Approach for Imperfection-Insensitive Thin-Shell Structure Design via Localized Dimple Imperfections and Gradient Boosting

Kyungmin Kim, Fabien Royer



Highlights

A Data-Driven Approach for Imperfection-Insensitive Thin-Shell Structure Design via Localized Dimple Imperfections and Gradient Boosting

Kyungmin Kim, Fabien Royer

- Data-driven framework for obtaining imperfection insensitive boom geometry
- Verified thin-shell boom more sensitive to localized imperfection than eigenmode imperfection
- Natural Gradient boosting (NGBoost) employed for skew normal buckling load distribution
- Multi-objective geometry optimization maximizing mean and minimizing standard deviation of buckling load

A Data-Driven Approach for Imperfection-Insensitive Thin-Shell Structure Design via Localized Dimple Imperfections and Gradient Boosting

Kyungmin Kim[a], Fabien Royer[a,*]

[a]*Sibley School of Mechanical and Aerospace Engineering, Cornell University, NY, United States of America*

Abstract

Thin-shell structures exhibit an unpredictable buckling behavior caused by their extreme sensitivity to localized imperfections. This work presents a data-driven framework to obtain imperfection-insensitive thin-shell structures based on an approach that replaces traditional eigenmode-based imperfection modeling with localized dimple imperfections. While the framework is general in nature, the study focuses on one particular kind of thin-shell structure, the Collapsible Tubular Mast (CTM), increasingly used in ultralight deployable space structures. When deployed, the structures experience a bending loading which can result in the boom buckling. A skew-normal distribution is shown to describe the distribution of resulting buckling moment when imperfections are seeded in the initial boom geometry, leading to the adoption of Natural Gradient Boosting (NGBoost) for probabilistic predictions under two bending directions. The models estimate mean and standard deviation of the buckling moment for varying boom design parameters, thereby capturing heteroscedastic uncertainty arising from geometric imperfections. Multi-Objective Optimization (MOO) techniques then integrate the predictive models to balance competing objectives, maximizing average buckling capacity while minimizing its variability. Results reveal distinct pareto-optimal designs that can achieve high buckling loads with reduced imperfection-sensitivity. This framework highlights the importance of local imperfection modeling and probabilistic data-driven methods in advancing

*Corresponding author

Email address: fabienr@cornell.edu (Fabien Royer)

robust thin shell design for next-generation deployable space systems.

Keywords: Thin-shell Structures, Imperfection-sensitivity, Collapsible Tubular Mast (CTM) Booms, Localized Dimple Imperfections, Natural Gradient Boosting, Multi-Objective Optimization

---

1. Introduction

Thin-shell structures, known for their high stiffness per mass, are widely used in demanding engineering applications such as aerospace, automotive, and military systems (1). Among thin-shell structures, deployable booms are increasingly employed in large, lightweight space structures to provide the stiffness required after deployment, while being highly packageable to fit in a rocket fairing (2; 3; 4; 5; 6). Recent studies have aimed to improve these boom designs to increase the performance of such space systems. However, the reduction in thickness makes them highly susceptible to instability such as buckling. Thinner structures exhibit heightened sensitivity to imperfections, which significantly amplifies their chaotic behavior. Therefore, accurately predicting buckling becomes exceedingly challenging, leading engineers to avoid operating near the theoretical buckling limit. The resulting design approaches rely on highly conservative safety factors, which severely limits mass efficiency of space structures, and consequently their size.

Considering the inherent unpredictability of buckling in thin-shell structures (7), understanding buckling behaviors has been a focal point of many investigations (8; 9; 10; 11). In 1941, Von Kármán and Tsien demonstrated the existence of an unstable post-buckling path in shells that, starting at the bifurcation point, eventually restabilizes at much lower loads (12). Koiter later theorized (13) that geometric imperfections resembling the first buckling mode result in the greatest reduction in buckling capacity, a theory validated by experiments on both shells with prescribed imperfections (14) and near-perfect shells (15). These findings led to the development of the knockdown factor method, which provides design guidelines for compressed cylindrical and spherical shells. Although advances in materials and manufacturing have inspired efforts to update knockdown method, the new criteria remain conservative, geometry-specific, and experimentally intensive (16). Recently, Abramovich (17) introduced the Vibration Correlation Technique (VCT) to estimate buckling loads non-destructively across a variety of thin-shell configurations, though this approach requires multiple tests for different loading

scenarios. Weisz-Patrault et al. (18) explored how residual stress influences post-buckling responses, leveraging both in-situ experiments and numerical simulations, yet this method was primarily examined for limited geometries.

Although these efforts provide valuable insights, they often rely on linear eigenvalue approaches and primarily consider global buckling modes, overlooking the critical role of buckling localization that can govern failure before any global mode does (19; 20; 21; 22). Thus, researches have been conducted to study the importance of localization in shell buckling, which was observed in multiple applications (6). Tvergarard and Needleman (23) showed that cylindrical panels undergo localized buckling soon after reaching peak load, while Groh et al.(24) demonstrated that single-dimple modes lower the energy barrier between pre- and post-buckling states—thereby increasing structural sensitivity to perturbations. Audoly et al. (25) further extended these insights by examining localization in spherical shells and found that such deformations tend to concentrate around particular regions (e.g., the poles). Therefore, researchers have recently focused on studying shells such as cylindrical shells (26; 27; 22; 28; 29) and spherical shells (30; 31; 32; 33; 34; 35; 36; 37), with highly localized imperfections, as a way to generate more accurate buckling predictions for real structures (5).

The Collapsible Tubular Mast (CTM) boom, a thin-shell deployable structure composed of joined omega-shaped walls, is increasingly employed in space applications due to its compactness and structural stability (38). Originally fabricated from metal sheets for the Viking 1 and 2 missions in 1976 (39), CTM booms have since advanced with the introduction of carbon fiber-reinforced polymer (CFRP) designs in the mid-1980s (40), spurring a wave of recent research. Lee et al. (41) developed an analytical model for two-shelled CTM booms to achieve bistability, showing that such designs require significantly lower strain energy to remain coiled and provide more predictable deployment. Palmeri et al. (42) introduced a design optimization framework aimed at enhancing structural performance while ensuring bistability, which was followed by a study on buckling load prediction using neural networks (43). Although these studies offer valuable insights into CTM boom design, they either assume imperfection-free models, or eigenmode-based imperfections, therefore overlooking the critical impact of buckling localization in real buckling load predictions.

In this work, we address the imperfection-sensitivity of CTM booms by introducing localized dimple imperfections as an alternative to traditional eigenvalue-based imperfection strategies. First, we illustrate how local dim-

ples yield more critical buckling scenarios than conventional eigenvalue imperfections, which justifies their use in imperfection-sensitivity predictions. Given the heteroscedastic nature in geometric imperfections, we adopt a stochastic modeling framework using Natural Gradient Boosting (NGBoost) (44) to correlate design parameters with buckling moments. Subsequently, this surrogate model is integrated into a multi-objective optimization, generating a Pareto front that highlights the trade-offs among key performance criteria. By combining localized imperfection modeling, probabilistic analysis, and data-driven design optimization, our approach aims to foster more robust and reliable thin-shell structures configurations for next-generation deployable space systems.

2. Methodology

2.1. Problem definition

Traditionally, classical buckling analyses for thin-shell structures rely on eigenvalue approaches (45; 46). Such methods identify critical loads and global buckling modes for perfect structures. These buckling modes are then scaled and seeded as geometric imperfections in the nominal structures to conduct post-buckling analyses using for instance an arclength solver. The evolution of the first limit load (transition into post-buckling) as the imperfection amplitude increases was also used as a way to quantify imperfection-sensitivity, through the computation of the buckling knockdown factor. While such methods are powerful, they have two principal limitations: (i) they do not fully account for the geometric imperfections encountered in real structures, and (ii) the resulting eigenmodes are only valid at the theoretical bifurcation point, which in practice is never reached. The structure always transitions at lower loads to localized buckling solutions (6).

More recent investigations incorporated localized dimple imperfections in cylindrical and spherical shells (24; 31). Our paper extends the use of dimple imperfections to thin-shell boom structures, where variation of imperfection location and and characteristics are a priority but not studied before. In this study, a single dimple was selected because previous studies demonstrated that the single dimple deformation corresponds to a mountain pass point in the energy landscape, which means this deformation mode features the lowest energy barrier separating unbuckled and buckled states (47). Therefore, this type of imperfection affects imperfection-sensitivity the most (35; 22).

For this, we first decided shape and location of dimple to be used for comparison between localized dimple imperfections and conventional eigenvalue-based imperfections for modeling the buckling response of booms. Figure 1 depicts the boom geometry and 2 indicates the manner in which the dimple imperfection is applied. The CTM design was selected for optimization, with R_1 and α chosen as the primary design parameters. The relationships between h, w, R_1, and α are defined as:

$$h = 2(w + L_1 + L_2) \tag{1}$$

$$L_{1,2} = R_{1,2}\,\alpha \tag{2}$$

while Table 1 outlines the parameter ranges and fixed values chosen for this study. Prior to applying the dimple imperfections, we conducted a standard eigenvalue analysis to examine the nature of the predicted buckling modes under two bending scenarios: an x-bending and a y-bending.

R_1 [mm]	α [°]	h [mm]	b [mm]	t [mm]	w [mm]
[20, 30]	[30, 50]	110	500	0.01	5

Table 1: Parameters applied for boom design

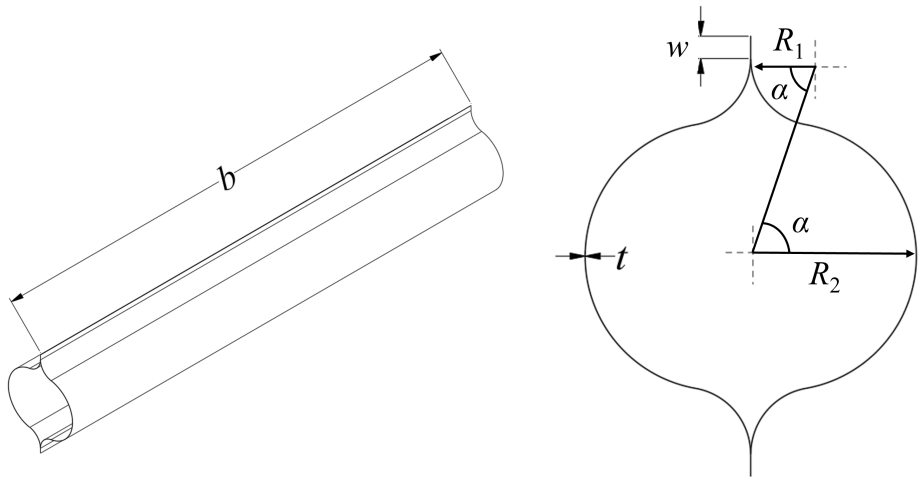


Figure 1: Schematic of employed boom design.

The boom material is linear elastic and isotropic with $E = 174.4GPa$ and $\nu = 0.26$, and a shell thickness is $t = 100\mu m$. The Young's modulus is chosen such that it matches with the longitudinal modulus of a carbon fiber reinforced polymer laminate commonly used to fabricate these booms (48). While these laminates are orthotropic, we focus here on an isotropic material for simplicity and ease of generalization, but further studies will explore the impact of lamination in fiber composites on the boom's imperfection-sensitivity. However, we expect this phenomenon to be primarily driven by geometry rather than material.

This study used the Abaqus/Standard (Implicit) finite element software to simulate boom buckling. The boundary conditions were applied via reference points which are rigidly coupled to all the nodes located on the boom's end cross-sections, as illustrated in Figure 2. For x-bending scenarios, x- and y-translations and y- and z-rotations were constrained for both reference points. To allow for the change in projected distance between the end cross-sections during bending, one reference point was left free to translate in the z-direction. In the case of y-bending, x- and y-translations and x- and z-rotations were constrained for both reference points, with one reference point again free to translate in the z-direction to accommodate projected distance change. A total of 12,024 reduced integration shell elements (S4R) were used to mesh the boom model throughout the entire simulation. This mesh density was obtained through a buckling load convergence test, and aligns with guidelines established in recent work on localized buckling (49).

As shown in Figure 2, buckling eigenmodes deformations under x-bending are predominantly found along the centerline of the boom, while those under y-bending are concentrated near the edges. Recent work indicated that for a perfect structure, localization of a single dimple occurs at the location of peak eigenmode deformations, and that the lowest buckling energy barrier is found at that location (50). It is therefore easiest for an imperfection to modify the buckling energy barrier and induce buckling at that location (49). Based on this observation, dimple imperfections were placed along the centerline for x-bending and near the edges for y-bending. Note that this choice aligns with the x-coordinate for which the maximum compressive stress is found under bending. The local dimple shape follows a two-dimensional Gaussian function characterized by an amplitude A, location parameter l, and standard deviation σ_{dimple}, representing the axial (z-direction) position of the peak and

the width of dimple, respectively as:

$$y = A \cdot \exp\left(-\frac{1}{2}\left[\left(\frac{x - l_x}{\sigma_{dimple}}\right)^2 + \left(\frac{z - l}{\sigma_{dimple}}\right)^2\right]\right) \tag{3}$$

For x-bending, the lateral position l_x was fixed at 0 to place the dimple along the centerline. For y-bending, l_x was defined as $-(R_1 + R_2) \cdot \sin(\alpha) + w$, ensuring that the dimple aligns with the boom edge. The dimple shape is applied to the upper surface of initial boom geometry through boundary conditions based on Gaussian distribution described above in a static general analysis. The resulting deformed geometry is then imported for the main buckling analysis.

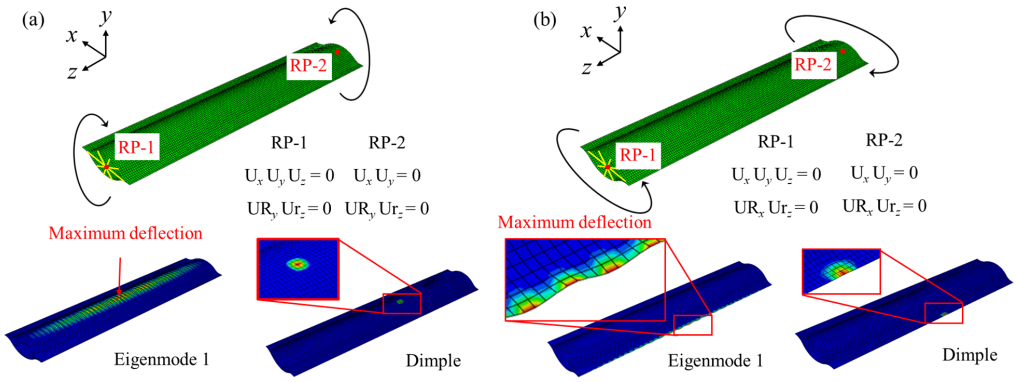


Figure 2: Buckling deformation by linear eigenvalue analysis and corresponding dimple imperfection when (a) x-bending and (b) y-bending are applied.

2.2. Choice of critical imperfection characteristics

To motivate the use of a localized dimple imperfection for imperfection-sensitivity computations, we conducted buckling and post-buckling simulations on imperfect structures featuring dimple imperfections, and compared their buckling responses to those obtained using eigenmode-based imperfections for a single boom design when $R_1 = 25\,mm$ and $\alpha = 37.5°$. The analysis is based on the comparison between the first eigenmode imperfection and a corresponding localized dimple imperfection. The first eigenmode was selected as it is traditionally seen as the most critical geometric imperfections (13). The dimple was positioned in the middle of the boom—corresponding

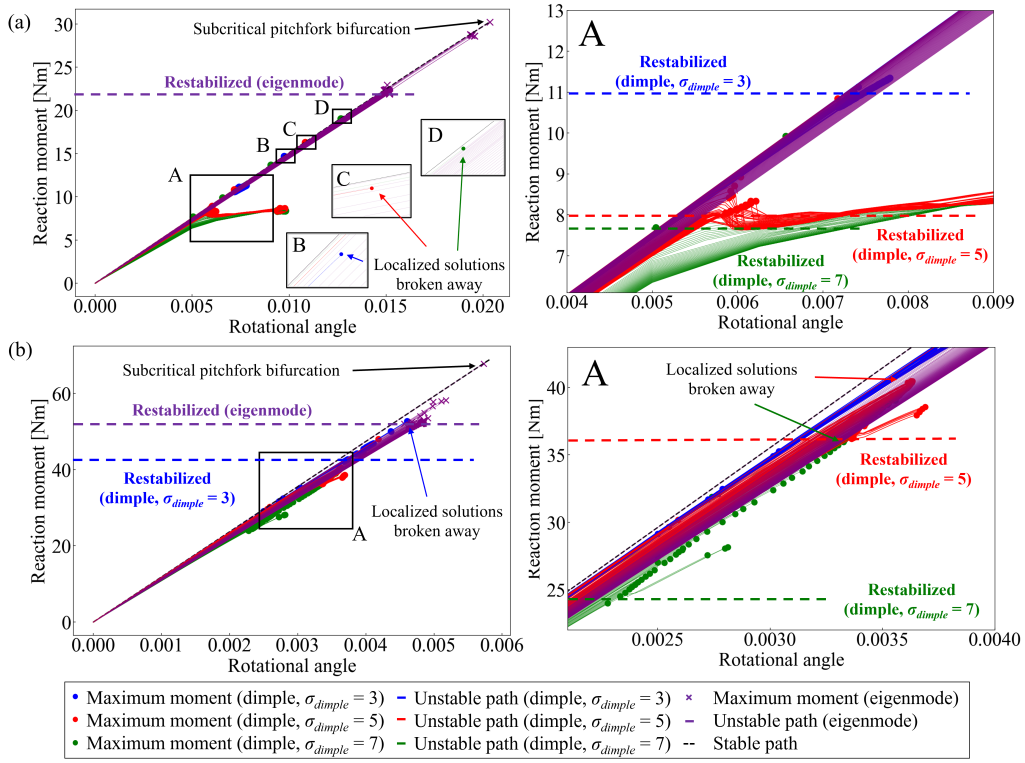
to the location of maximum deflection in the first eigenmode—for both x- and y-bending cases, as indicated in Figure 2. To investigate the influence of dimple width on the buckling behavior, additional simulations were performed by varying the standard deviation σ_{dimple} of the Gaussian function defining the dimple shape. The ranges of dimple amplitude and width were chosen such that the buckling response spans the whole range of behavior from bifurcation to the full stable formation of post-buckling deformations. In total, 60 simulations were conducted for each imperfection.

Figure 2.2 (a) and (b) illustrate the results. In both plots, the bifurcation point of the unstable path based on the eigenmode imperfection is shown as a subcritical pitchfork bifurcation. Additionally, the limit points of the unstable paths resulting from localized dimple imperfections, representing localized solutions broken away from the stable path (24), are highlighted in zoomed-in boxes B, C, and D in Figure 2.2 (a), and box A in Figure 2.2 (b). The lowest buckling moments along each unstable path, referred to as restabilized values, are indicated by dotted lines in both figures.

In both bending scenarios, the behavioral differences between eigenmode (global) and dimple (localized) imperfections previously discussed in (24) were clearly observed. Structures with eigenmode imperfections exhibited a rapid drop in reaction moment associated with subcritical pitchfork bifurcation, branching from the stable equilibrium path of the ideal (perfect) structure. In contrast, localized solutions are broken-away from the stable pre-buckling path and do not intersect it, which makes them impossible to detect with a classical eigenvalue analysis. Notably, the unstable paths associated with dimple imperfections exhibit a consistently lower range of reaction moment for the same imperfection amplitude compared to those with eigenmode imperfections, regardless of dimple width. This indicates that structures with localized imperfections are more prone to earlier transition into buckling as indicated in previous study (19). As the dimple width increases, the point at which the post-buckling response restabilization decreased for both x- and y-bending. In case of x-bending, the moment where buckling response restabilization converges after σ_{dimple} gets larger than 5 mm. Thus, we selected $\sigma_{dimple} = 5$ mm for this study.

Thin shell structures are well known to be susceptible to buckling than their thicker counterparts. To further investigate the influence of thickness on the buckling behavior of the boom and to emphasize the significance of localized imperfections in thin shell structures, we repeated the analysis with an increased thickness of $0.5\,mm$ ($R/t = 50$), which is 50 times greater than the

original value. The results are shown in Figure 3. The overall trends remain consistent, which further reinforces what observed in Figure 2.2. However, a notable shift was observed with increased thickness: the hierarchy of reaction moments between the two imperfection types was reversed. While localized imperfections played a dominant role to the lower reaction moment in the thinner configuration, the thicker structure showed that eigenmode imperfections became comparatively more critical. This observation underscores the heightened sensitivity of thin shell structures to localized imperfections and highlights the necessity of accounting for such defects when designing for structural stability under thin-shell conditions.



Comparison of buckling behavior between the first linear eigenmode imperfection and a corresponding localized (middle dimple) imperfection when $t = 0.01\,mm$ $(R/t = 2500)$ under (a) x-bending and (b) y-bending. The right-hand plots represent the zoomed-in box A for clarity. In both cases, the boom exhibits higher sensitivity to localized imperfections than eigenmode imperfections.

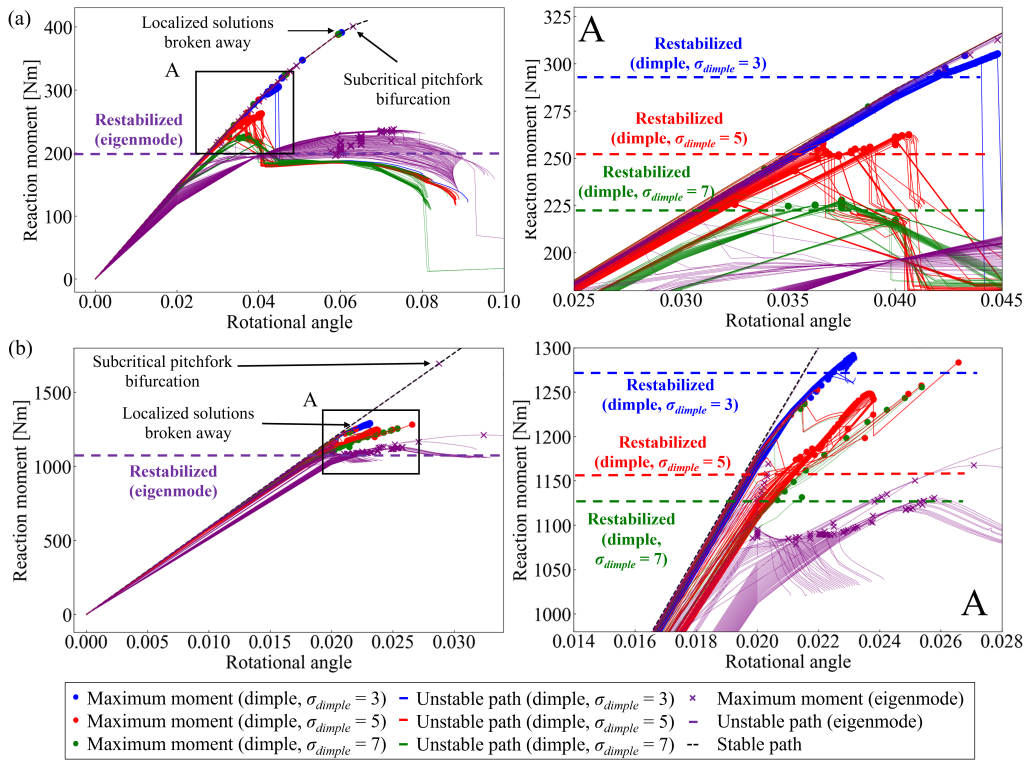


Figure 3: Comparison of buckling behavior between the first linear eigenmode imperfection and a corresponding localized (middle dimple) imperfection when $t = 0.5\,mm$ $(R/t = 50)$ under (a) x-bending and (b) y-bending. The right hand plots represent the zoomed-in box A for clarity. The hierarchy of reaction moments between the two imperfection types was reversed compared to lower thickness, which underscores the higher sensitivity of thin shell structures to localized imperfections than thicker structures.

2.3. Imperfection-sensitivity induced buckling load stochasticity

Measuring localized imperfections in shell structures poses a significant challenge, particularly for very thin-shell structures where stringent manufacturing tolerances are difficult to maintain (51). In practice, even imperceptible imperfections can have a dramatic effect on buckling. Because it is impractical to measure the shape of large structures with a high level of accuracy and precision, a stochastic treatment of imperfections is necessary to capture their influence on the buckling response. To this end, we examined how variations in localized dimple imperfection parameters affect the distribution of the resulting buckling moment.

In this study, two dimple parameters, amplitude (A) and location (l), were selected to characterize geometric imperfections. A total of 100 parameter pairs (A_i, l_i) were generated using a Sobol sequence (52; 53). The Sobol sequence is a quasi-random low-discrepancy sequence that generates sample points more uniformly than purely random methods. It constructs each point using base-2 digital operations that ensure an even distribution across the parameter space. This method produces a non-uniform, space-filling design of experiments (DoE) that is particularly well-suited for data-driven modeling (54). The parameter ranges are provided as:

$$A = [-0.5,\, 0.5]\, mm, \quad l = [50,\, 250]\, mm \tag{4}$$

and Figure 4 illustrates the resulting sample distribution.

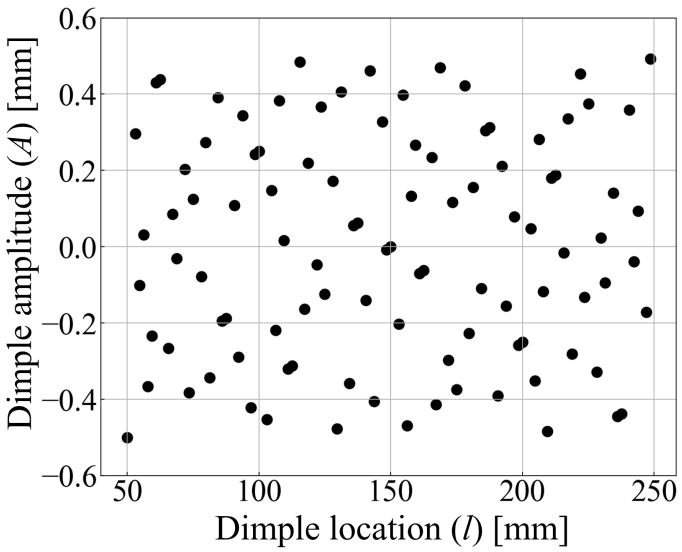


Figure 4: Sampling of imperfection parameters using a Sobol sequence.

Next, we applied the sampled imperfection parameters to a single boom configuration with $R_1 = 25\, mm$ and $\alpha = 37.5°$. The resulting spread in buckling moments for both x- and y-bending cases is shown in Figure 5. To model the observed asymmetry in the distributions, several statistical models can be considered, such as the Weibull distribution which has been effective in modeling the impact of imperfections on buckling loads (55; 56; 57). Here we chose to use the skew normal distribution (58), as a starting point, given its

compatibility with NGBoost and ease of implementation. The skew normal distribution extends the conventional normal distribution by introducing a shape parameter that captures skewness (59), but a thorough comparison between predictions generated with the Weibull distribution and skew normal distribution could be an insightful extension of this work. Furthermore, additional simulations would improve the fit between skew normal distribution and buckling moment statistics. However, it is important to mention that the distribution parameters change with the input geometry and the data-driven model aim to predict these parameters even in a data-constrained environment. The probability density function for a continuous random variable X with skewed normal behavior is summarized as:

$$f(x) = \frac{2}{\omega}\phi\left(\frac{x-\xi}{\omega}\right)\Phi\left(\alpha\left(\frac{x-\xi}{\omega}\right)\right). \tag{5}$$

where ξ, ω and α represent the location, scale, and shape parameters, respectively. The mean μ and standard deviation σ are computed from these parameters as:

$$\begin{aligned} \mu &= \xi + \omega\delta\sqrt{\frac{2}{\pi}}, \\ \sigma &= \omega\sqrt{1-\frac{2\delta^2}{\pi}} \end{aligned} \tag{6}$$

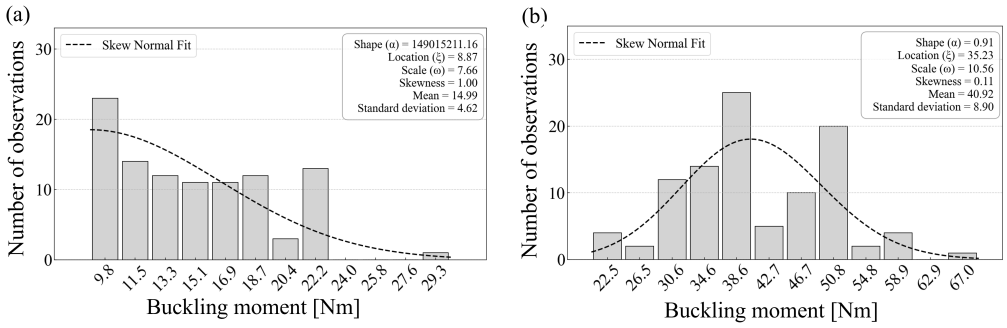


Figure 5: Number of buckling moment observations for a dimple imperfection, for (a) x-bending and (b) y-bending applied. Each panel includes the fitted skew normal distribution with its location, scale, and shape parameters. Approximately 5 hours of simulation time was required to generate each distribution

2.3.1. Natural Gradient Boosting for heteroscedastic noise

Thin-shell structures, such as CTM booms, are known to be highly sensitive to imperfections, leading to significant variability in their buckling moment (60). What complicated the analysis of this imperfection-sensitive behavior is the fact that the statistical distribution of buckling moments depends on the geometric input parameters. This phenomenon is termed heteroscedasticity (61). For instance, as demonstrated in Appendix B, applying the same set of imperfection parameters used in Figure 5 to different geometric configurations results in distinct buckling moment distributions. This variation, induced by changes in geometry, introduces heteroscedastic noise.

Gaussian Process Regression (GPR) has been extensively applied to heteroscedastic data due to its proven ability to capture underlying uncertainties (62) and its capacity to model varying residual variances (63). However, GPR typically assumes noise that is independent and identically distributed (i.i.d.) and normally distributed, rendering it unsuitable for the skewed noise distribution observed in the dimple imperfection data (see Figure 5). To address this limitation, we employ Natural Gradient Boosting (NGBoost) (44), which offers a flexible framework for probabilistic predictions under a variety of distribution families.

NGBoost extends traditional Gradient Boosting (64), a powerful ensemble learning technique that builds a strong predictive model by sequentially combining multiple weak learners—typically shallow decision trees. NGBoost has significantly lower training time than GPR, especially on large datasets, as it avoids the cubic time complexity of GPR's kernel matrix inversion. In each iteration of gradient boosting, a new weak learner is trained to predict the residual errors (i.e., the negative gradients of the loss function) of the ensemble model built so far. These learners are added to the ensemble in a stage-wise manner to progressively reduce the overall prediction error and minimize a chosen loss function.

NGBoost generalizes this framework by modeling not just point estimates but full probability distributions $P(y \mid x)$. This probabilistic perspective enables the estimation of both predictions and their associated uncertainty. Rather than optimizing a scalar loss, NGBoost minimizes a proper scoring rule over distributions, such as the negative log-likelihood employed in this study. The update step uses a natural gradient, defined as:

$$\widetilde{\nabla} S(\theta, y) \propto \lim_{\epsilon \to 0} \arg \max_{d: D_S(P_\theta \| P_{\theta+d}) = \epsilon} S(\theta + d, y) \tag{7}$$

where S is the score function, d is the direction vector, D_S is the divergence, and P_θ is the probability distribution corresponding to the current parameter θ. By descending along the negative natural gradient, NGBoost iteratively refines the predicted distribution to minimize the scoring rule, offering a robust and theoretically grounded approach to uncertainty-aware prediction.

Unlike standard GPR, NGBoost can accommodate diverse distributions; here, we define a custom skew normal distribution with parameters $\theta = (\alpha, \mu, \sigma)$ to capture the shape, mean, and standard deviation of the skewed noise. The outputs at each boosting stage are scaled by stage-specific factors $\rho^{(m)}$ and a common learning rate η (Equation 8), where $f^{(m)} = \left(f_\alpha^{(m)}, f_\mu^{(m)}, f_\sigma^{(m)}\right)$ represents the set of base learners in each stage m.

$$y \mid x \sim P_\theta(x), \quad \theta = \theta^{(0)} - \eta \sum_{m=1}^{M} \rho^{(m)} \cdot f^{(m)}(x) \tag{8}$$

3. Optimization of boom design

3.1. Optimization framework

Figure 6 presents the four-step optimization framework, inspired from the work of Bessa and Pellegrino (65). The framework consists of: 1) Data Sampling, 2) Computational Analysis, 3) Probabilistic Prediction, and 4) Optimization. While the general structure follows that of Bessa and Pellegrino, the present work is fundamentally different as it focuses on localized buckling solutions (broken away from the pre-buckling path) rather than eigenmode-based solutions (connected to the pre-buckling path through bifurcations). While the distinction may sound subtle, it dramatically changes the analysis since there exists an infinite number of localized imperfections leading to broken-away solutions while there is only a handful of eigenmodes at most found close to the first bifurcation point. For this reason, Bessa and Pellegrino focused on the impact of eigenmode-imperfections on the ultimate buckling load rather than the first buckling load, since a simple iteration on the eigenmode amplitude would yield similar results. In our case, there is potentially an infinite number of imperfections to consider, which makes the data-driven framework particularly suitable to study the first buckling load. In addition, we introduced a NGBoost model to more accurately model the imperfection sensitivity of the boom. In the Data Sampling step, we generate simulations across three dimensions (**i**,**j**,**k**), where **i** denotes the loading

condition, **j** indexes geometric parameters, and **k** represents imperfection parameters. In this study, $\mathbf{i} = 2$ corresponds to the number of loading cases, here x- and y-bending. We set $\mathbf{j} = 50$ for 50 different (R_1, α) combinations within the ranges given in Table 1, and $\mathbf{k} = 10$ for the dimple imperfection parameters in Equation 4 using the Sobol sequence shown in Appendix A. This yields $2 \times 50 \times 10 = 1000$ finite element (FE) simulations, which required approximately two weeks of continuous computation using a dual-core processor. All simulations were performed via in-house automation scripts that interface with the Abaqus/Implicit solver.

After obtaining the buckling moments from the FE simulations, we employed NGBoost to establish a probabilistic predictive model. By relating the geometric parameters (R_1, α) to the observed buckling moments, we sought to estimate both the mean μ and standard deviation σ of the response distribution for each geometry.

Before training the final NGBoost models, hyperparameter tuning was conducted using a Grouped k-fold Bayesian optimization approach. We adopted grouped k-fold cross-validation (CV) (66) to avoid overfitting (67; 68), leveraging a limited dataset more effectively (69). Specifically, each group consisted of the 10 imperfection variations associated with a single geometry, and the 50 geometries were partitioned into five folds for CV. We optimized the number of estimators n and the learning rate η based on minimizing the mean squared error (MSE). The evolution of the MSE as a function of the iteration number is shown in Appendix A. For the x-bending dataset, the optimal values were $n = 292$ and $\eta = 0.0051$; for the y-bending dataset, $n = 145$ and $\eta = 0.0071$

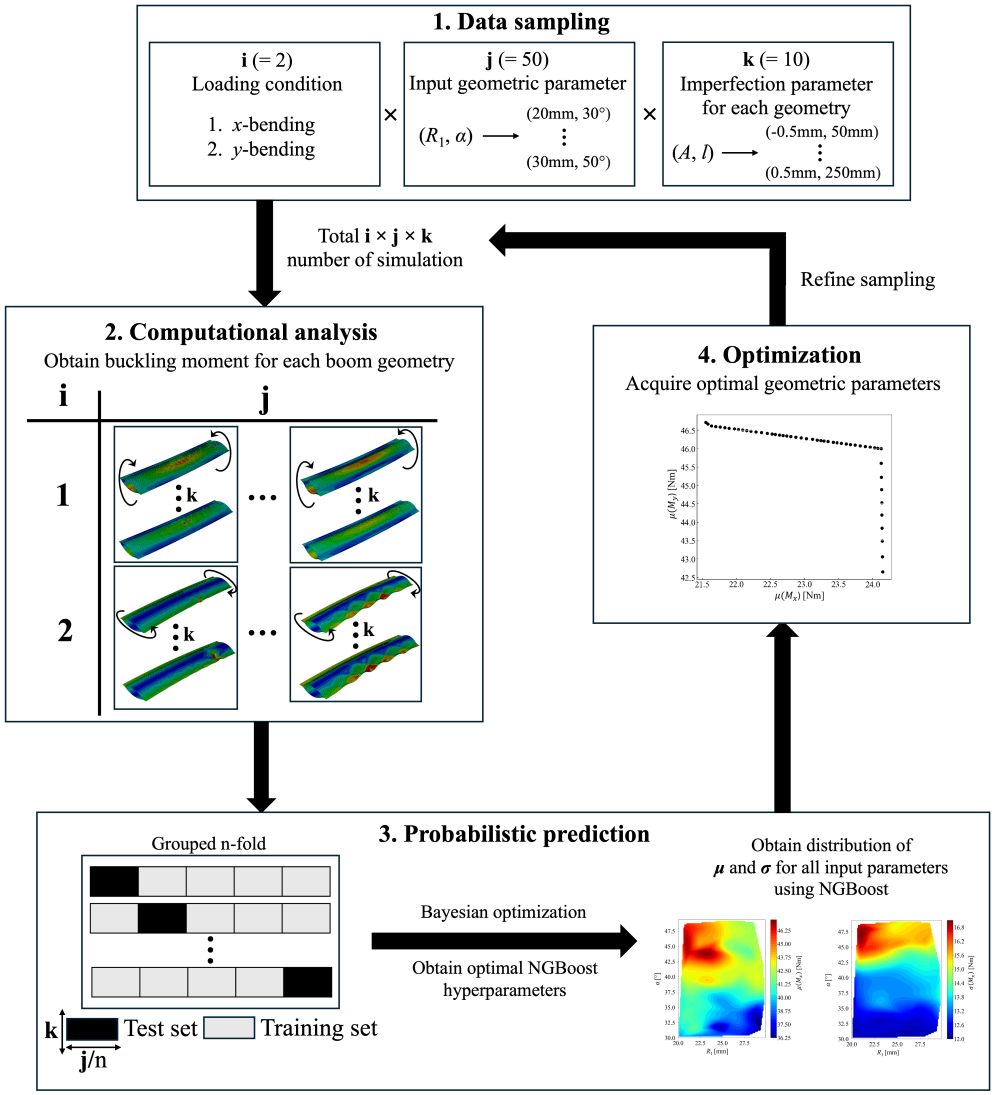


Figure 6: Flow chart of optimization framework modified from Bessa et al. (65)

Using obtained hyperparameters, we then trained separate NGBoost models for x- and y-bending. The model outputs (mean, standard deviation) for each set of geometric parameters were linearly interpolated to visualize trends in the predicted mean and standard deviation of the buckling moment, as shown in Figure 7. When the boom was subjected to x-bending, increasing α generally increases predicted mean $\mu(M_x)$, whereas R_1 has a relatively

modest influence. The $\mu(M_x)$ values range from a maximum of 23.75 Nm to a minimum of 12.5 Nm, representing an approximate 50% decrease across the design space. The standard deviation $\sigma(M_x)$ has value ranging from 9.84 Nm to 6.24 Nm—an approximate 25% reduction, exhibiting a noticeable dip around $\alpha \approx 32.5°$. Under y-bending, the $\mu(M_y)$ peaks around two regions: approximately at $(R_1, \alpha) \approx (22.5\,mm, 43°)$ and $(21\,mm, 45°)$, and reaches a minimum near $(R_1, \alpha) \approx (30.5\,mm, 33°)$. $\sigma(M_y)$ shows its peak around $(R_1, \alpha) \approx (20.5\,mm, 47°)$ and remains comparatively lower across most of the design space. For y-bending, the $\mu(M_y)$ ranges from 46.25 Nm to 36.25 Nm while $\sigma(M_y)$ ranges from 16.8 Nm to 12 Nm, both reflecting approximately 25% reduction.

Since a high buckling capacity is desirable for structural stability (70), one optimization target is maximizing the mean of the buckling moment μ. At the same time, reducing σ mitigates imperfection-sensitivity leading to a stochastic buckling behavior. Consequently, we perform a multi-objective optimization in the next stage to simultaneously maximize μ and minimize σ.

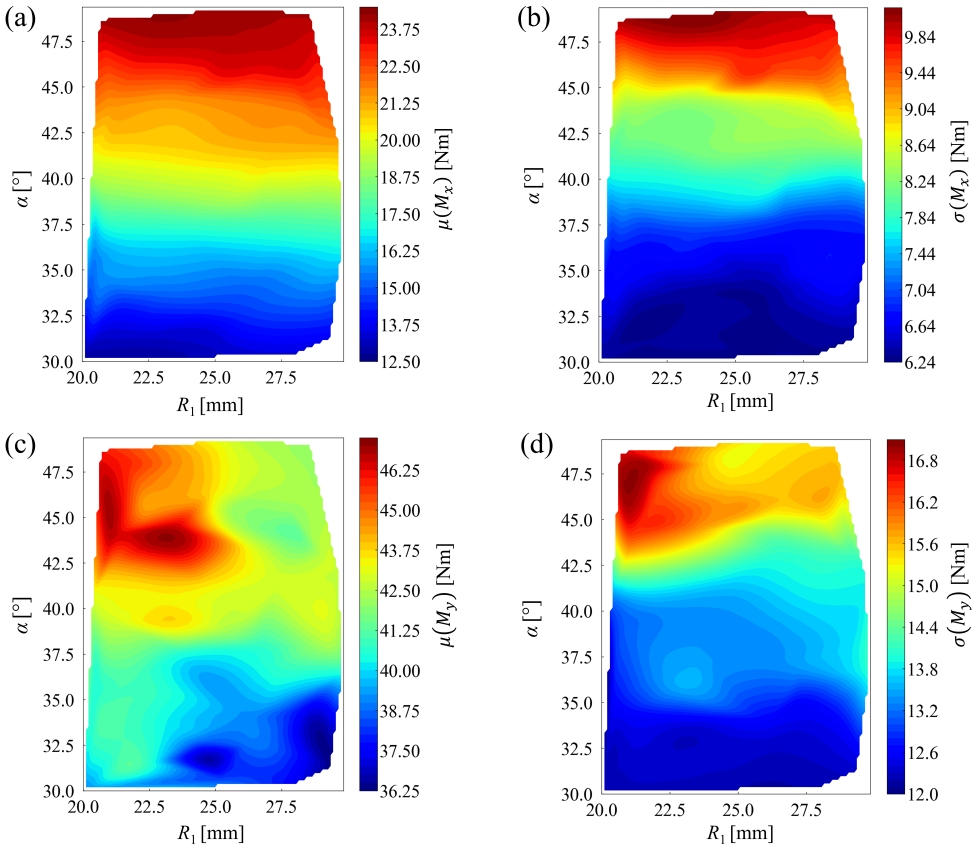


Figure 7: Distribution of (a) mean and (b) standard deviation of buckling moment under x-bending, and (c) mean and (d) standard deviation of buckling moment under y-bending.

3.2. Multi-objective Optimization

Multi-objective optimization (MOO) is employed to address problems involving two or more competing objectives under specific constraints (71). Such problems are formally defined by an objective function vector $\mathbf{F}(\mathbf{X})$ that must be either minimized or maximized over the decision variables $\mathbf{X}$. Each objective function represents a separate, computable criterion, and MOO requires at least two criteria to be optimized (72). The decision variables, R_1 and α in this study, are the independent numerical values directly influencing these objective functions.

Upon solving a MOO problem, a Pareto-optimal set (or Pareto front) emerges—those solutions that are non-dominated within the feasible design

space S (73).A solution S_1 dominates another S_2 if (74):

1. Solution $S2$ is not strictly better than $S1$ in any of the considered objectives.
2. Solution $S1$ performs better than $S2$ in at least one objective.

Because it is usually impossible to improve all objectives simultaneously, the Pareto front expresses a trade-off: any point on the front is at least partially optimal, yet each solution is inferior to another on at least one objective (75). In this study, the design variables R_1 and α influence two objectives: (i) maximizing the mean buckling moment (to increase overall structural capacity), and (ii) minimizing uncertainty (standard deviation) due to imperfections (to reduce performance variability).

To handle these objectives, we employed three MOO algorithms that are implemented using the python MOO library Pymoo (76) with default parameters: the Non-dominated sorting Genetic Algorithm II (NSGA-II) (71), Unified Non-dominated sorting Genetic Algorithm III (U-NSGA-III) (77), and $\mathcal{S}$ Metric Selection Evolutionary Multi-objective Optimization Algorithm (SMS-EMOA) (78), which have been proven effective in bi-objective optimization problem as in this study.

We first examine the Pareto fronts generated when maximizing the mean buckling moment under both $x-$ and $y-$bending. Although all three optimization algorithms (NSGA-II, U-NSGA-III, and SMS-EMOA) yield similar outcomes, we focus on the SMS-EMOA results for clarity, owing to its relatively uniform solution distribution. Figure 8(a) shows the resulting Pareto front after 500 generations from an initial population of 50 individuals. Here, M_x and M_y denote the buckling moments under x- and y-bending, respectively, and bracketed values indicate the geometric parameters (R_1, α) corresponding to points on the Pareto front.

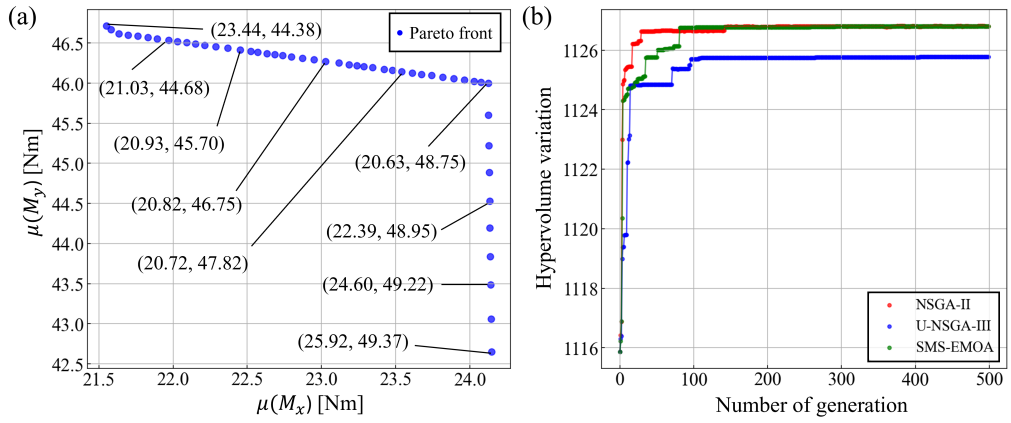


Figure 8: (a) Pareto front obtained from SMS-EMOA by maximizing mean value of buckling moment for x and y-bending and (b) hypervolume convergence metric of three optimization algorithms applied.

Notably, a discontinuity in slope occurs around $\mu(M_x) \approx 23.7$ Nm, suggesting a sharp transition in the trade-off space. Small variation in geometry around corresponding decision variables $(R_1, \alpha) \approx (20.63\,mm,\ 48.75°)$ changes the weight of either $\mu(M_x)$ or $\mu(M_y)$ in optimized point critically. Examining the corresponding decision variables on the Pareto front, we observe that R_1 consistently decrease when $\mu(M_x)$ increases until it reaches a transition point near $\mu(M_x) \approx 24.2$, while α increases. This behavior can be explained by examining Figure 7 (a) and (c), which reveal two distinct peaks in $\mu(M_y)$: the first near $R_1 = 24\,mm$ and the second around $R_1 = 21\,mm$. Since the first peak occurs further from the peak of $\mu(M_x)$ in design space, optimal designs shift from the first peak region toward the second peak region. Consequently, R_1 decreases from approximately $24\,mm$ to $21\,mm$, while α increases from about 40° to 44°. Beyond the transition point, both R_1 and α increase again, converging toward the peak of $\mu(M_x)$ at $(R_1, \alpha) \approx (25.92\,mm,\ 49.37°)$.

Figure 8 (b) shows the hypervolume evolution for each algorithm when reference point is set to (0,0) (79). The hypervolume is a commonly used performance metric in multi-objective optimization that measures the volume of the objective space dominated by the obtained Pareto front, relative to a predefined reference point. A larger hypervolume indicates better convergence and diversity of solutions (80). SMS-EMOA demonstrates the fastest convergence, reaching near-optimal solutions within roughly 100 gen-

erations. NSGA-II follows closely in convergence speed but incurs higher computational costs per generation and yields less uniform solutions than SMS-EMOA. U-NSGA-III exhibits the slowest convergence and lowest hypervolume due to its reliance on predefined reference directions (77). Increasing the number of reference directions can improve uniformity but introduces convergence challenges as a trade-off.

Next, to account for the influence of imperfections, we maximize mean minus standard deviation ($\mu - \sigma$); a metric representing a 68% confidence interval for the lower bound on buckling moments to balance high mean buckling capacity with imperfection-sensitivity. The resulting Pareto front (Figure 9(a)) follows a similar trend to the mean-only optimization, that R_1 decrease and α increase until slope transition point when $(\mu-\sigma)(M_x) \approx 14.1$ Nm. However, the values for $(\mu-\sigma)(M_y)$ decrease more significantly because the peak in $\mu(M_y)$ around $R_1 = 21\,mm$ mm coincides with a high $\sigma(M_y)$, as depicted in Figure 7. Figure 9 (b) demonstrates that SMS-EMOA maintains the fastest convergence, while both U-NSGA-III and NSGA-II show relatively improved performance compared to the mean-only optimization scenario.

Lastly, to minimize sensitivity to imperfections, we consider an objective that strictly minimizes the standard deviation of the buckling moment. Figure 10 (a) displays the resulting Pareto front, where the range of $\sigma(M_x)$ values is significantly lower than $\sigma(M_y)$. This distinction arises because the lower value regions of $\sigma(M_x)$ extensively overlap with those of $\sigma(M_y)$, as illustrated in Figure 7 (b) and (d). Thus, we can say that the geometric parameters $(R_1, \alpha) = (20\,mm, 30^\circ)$ minimize the standard deviation under both bending conditions, achieving $(\sigma(M_x), \sigma(M_y)) \approx (6.24, 12)$ Nm. Figure 10 (b) depicts hypervolume evolution based on a reference point of $\sigma(M_x) = 10$ Nm and $\sigma(M_y) = 17$ Nm, suitable for minimization problems. In this scenario, U-NSGA-III demonstrates the fastest convergence, followed by SMS-EMOA and NSGA-II.

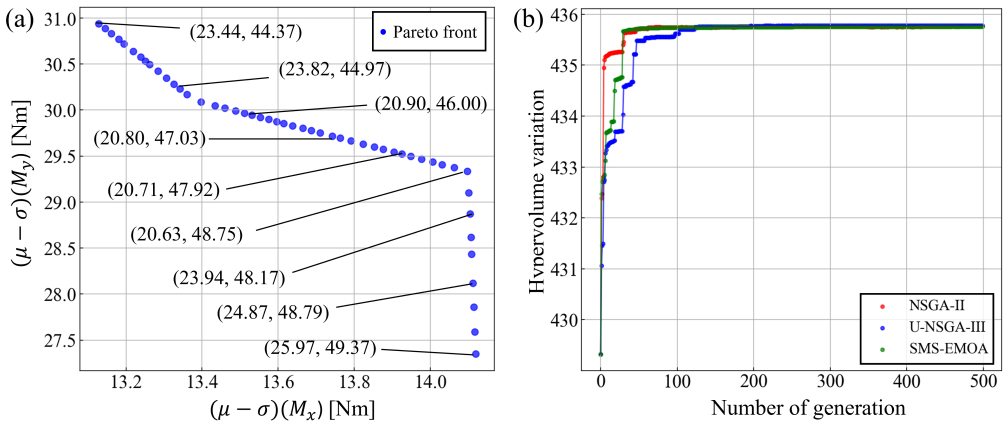


Figure 9: (a) Pareto front obtained from SMS-EMOA by maximizing mean minus standard deviations for x and y- buckling moments and (b) hypervolume convergence metric of three optimization algorithms applied.

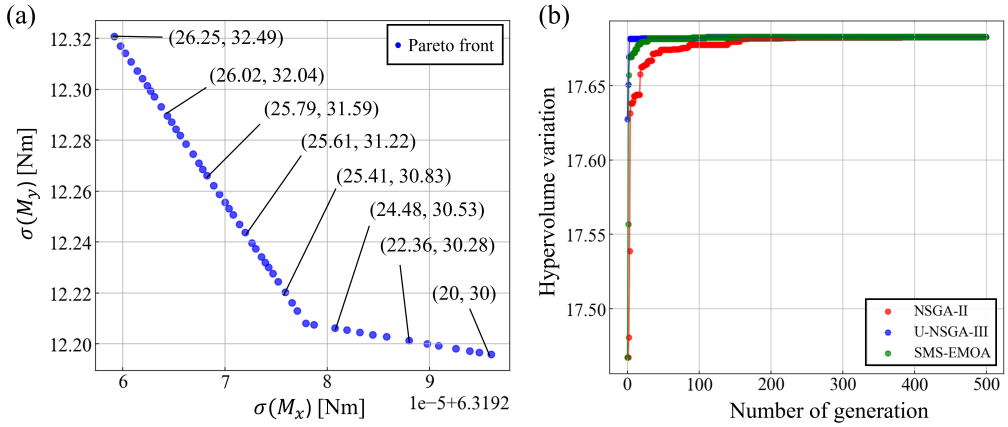


Figure 10: (a) Pareto front obtained from SMS-EMOA by minimizing standard deviation of buckling moment for x and y-bending and (b) hypervolume convergence metric of three optimization algorithms applied.

The three evolutionary optimization algorithms provide valuable design guidelines for CTM booms by accounting for stochastic localized imperfections. For example, based on the results shown in Figure 8(a), a designer may choose the geometric configuration $(R_1, \alpha) \approx (20.63\text{mm}, 48.75°)$. In this region, a small increase in the buckling moment under x-bending can lead

to a sharp decrease in the buckling moment under y-bending. This effect is due to the slope transition caused by the secondary peak observed in the y-bending moment distribution, as shown in Figure 7(c).

In this study, we considered only two bending conditions as optimization objectives. However, additional loading conditions can be included to produce a more comprehensive optimization landscape, despite the increased computational cost. For instance, z-bending (torsional loading) may be a suitable candidate. In such cases, multi-objective optimization algorithms that support more than three objectives can be employed to generate a three-dimensional Pareto front. This approach can provide more general design guidelines that account for a wider range of bending scenarios.

The differences observed in the Pareto fronts, depending on the selected optimization objectives, emphasize the importance of carefully choosing objective functions. These functions should reflect the desired design trade-offs, whether they focus on maximizing performance, minimizing uncertainty, or achieving a balance between the two. For instance, when comparing Figures 8 and 9, an additional slope change appears near $(R_1, \alpha) \approx (20.96\text{mm}, , 45.36^\circ)$, resulting in a slight increase in slope. This suggests that $R_1 = 20.96\,mm$ and $\alpha = 45.36^\circ$ may be a promising design candidate, as a modest increase in the y-bending moment could lead to a substantial reduction in the x-bending moment, depending on the design priorities.

4. Conclusion

In this study, we developed a data-driven framework to enhance thin-shell structure designs by accounting for localized geometric imperfections and the stochastic buckling response they lead to. We employed localized dimple imperfections in place of conventional eigenmode imperfections, and used NGBoost to model the skew-normal distribution of the resulting buckling moments variation. The framework then combined these probabilistic predictions with MOO techniques to identify Pareto-optimal boom geometries for two distinct loading directions.

Our comparison between localized dimple and eigenmode-based imperfections confirms that traditional eigenvalue analyses often underpredict the buckling imperfection sensitivity of thin-shell structures (81). These findings highlight the critical importance of accounting for imperfections, particularly localized ones, in the buckling analysis of thin-shell structures. This underscores the need for future studies to revisit critical localized imperfections

characteristics leading to the worst buckling responses, especially given that several recent works have been conducted under imperfection-free conditions (42; 43) or have considered only eigenmode-based imperfections (82; 83).

Employing three different MOO formulations for maximizing the mean buckling capacity, maximizing mean minus standard deviation, and minimizing the standard deviation, resulted in distinct sets of optimal geometries. This highlights the critical importance of clearly defining design objectives based on the intended performance criteria. Among the optimization algorithms, SMS-EMOA demonstrated the most uniform solution distribution along the Pareto front and the fastest convergence of the hypervolume, except in the case of minimizing the standard deviation.

This study primarily focuses on the optimization framework for the CTM boom, given its increasing application in deployable aerospace structures. However, building on the foundational insights from previous research, such as the significance of localized buckling in thin cylindrical (23; 24) and spherical shells (25; 26) as well as the application of pareto front optimization to various types of thin-shell booms (65), we believe that the proposed framework can be effectively extended to a wide range of structures exhibiting thin-shell characteristics.

Future work will focus on experimentally validating that geometries identified on the Pareto front indeed exhibit higher stability under the considered loading conditions. Moreover, exploring material imperfections can help refine the predictive accuracy of real-world boom configurations. Extending the framework to include post-buckling effects would offer a more comprehensive view of stability throughout the entire non-linear load-displacement response.

Appendix A. Bayesian optimization for NGBoost hyperparameter tuning

Using the geometric and imperfection parameters sampled via the Sobol sequence (Figure A.1), we performed a Bayesian optimization procedure to identify optimal hyperparameters for NGBoost. This framework computes both the mean and standard deviation of the buckling moment for each boom geometry. Because each geometry is associated with 10 different imperfections, we employed Grouped k-fold cross-validation to guarantee that same geometries are included in same fold. Specifically, each fold contained 10

geometries—40 geometries were used for training and 10 for testing in each iteration. The Scaled MSE served as our scoring function:

$$Scaled\ MSE = \left\{ \frac{(y - \mu)}{\sigma^2} \right\}^2 \tag{A.1}$$

where y is the true buckling moment, μ is the predicted mean buckling moment, and σ is the predicted standard deviation of buckling moment of the boom geometry. Minimizing this metric ensures both an accurate prediction of the mean and a sensible distribution width (i.e., avoiding an overconfident model that underestimates uncertainty). Figure A.2 shows the Scaled MSE values throughout the Bayesian optimization. For x-bending, the lowest average Scaled MSE over the test set occurred at iteration 292; for y-bending, the best was found at iteration 145. The corresponding hyperparameters from these iterations were then adopted, as reported in Section 3.1.

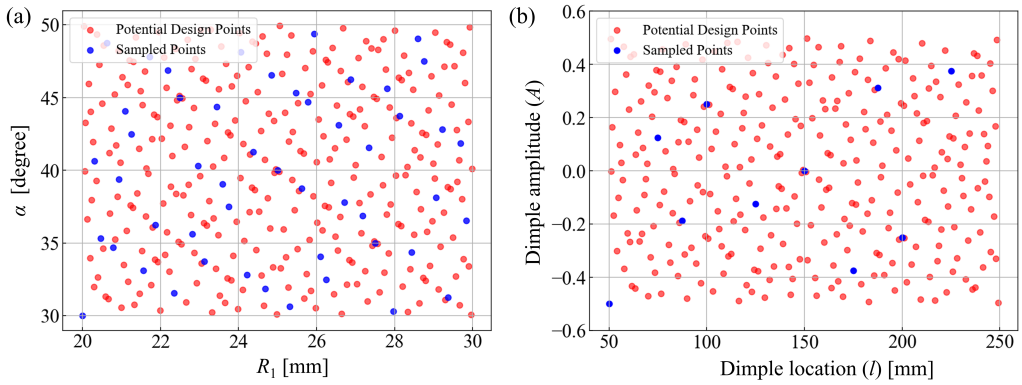


Figure A.1: Sobol sequence for obtaining (a) geometric parameters and (b) imperfection parameters for multi-objective optimization.

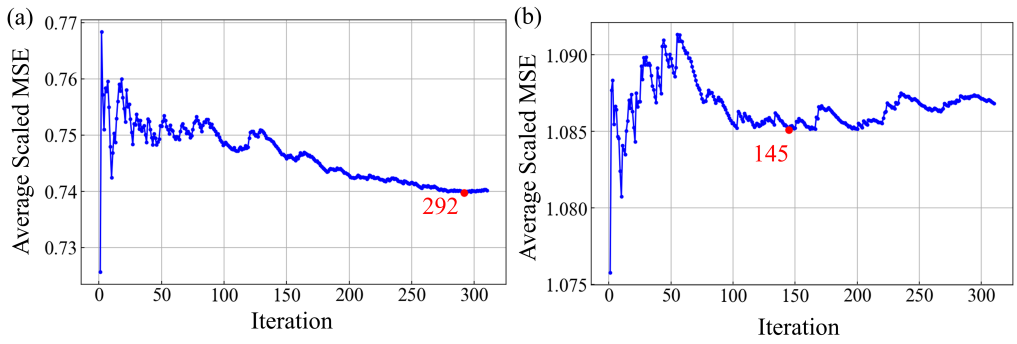


Figure A.2: Variation of Average Scaled MSE over iterations during Bayesian optimization for NGBoost hyperparameter tuning in case of (a) x- and (b) y-bending.

Appendix B. Heteroscedastic noise in buckling moment distribution

As discussed in section 2.3.1, the buckling moment distribution changes with variations in the input geometry. Figure B.1 illustrates how the number of buckling moment observations differs for dimple imperfections as the boom geometry varies, when same imperfection parameters are applied. Due to the heteroscedastic noise introduced by the imperfections, the probability density function of the skew-normal distribution changes with the input.

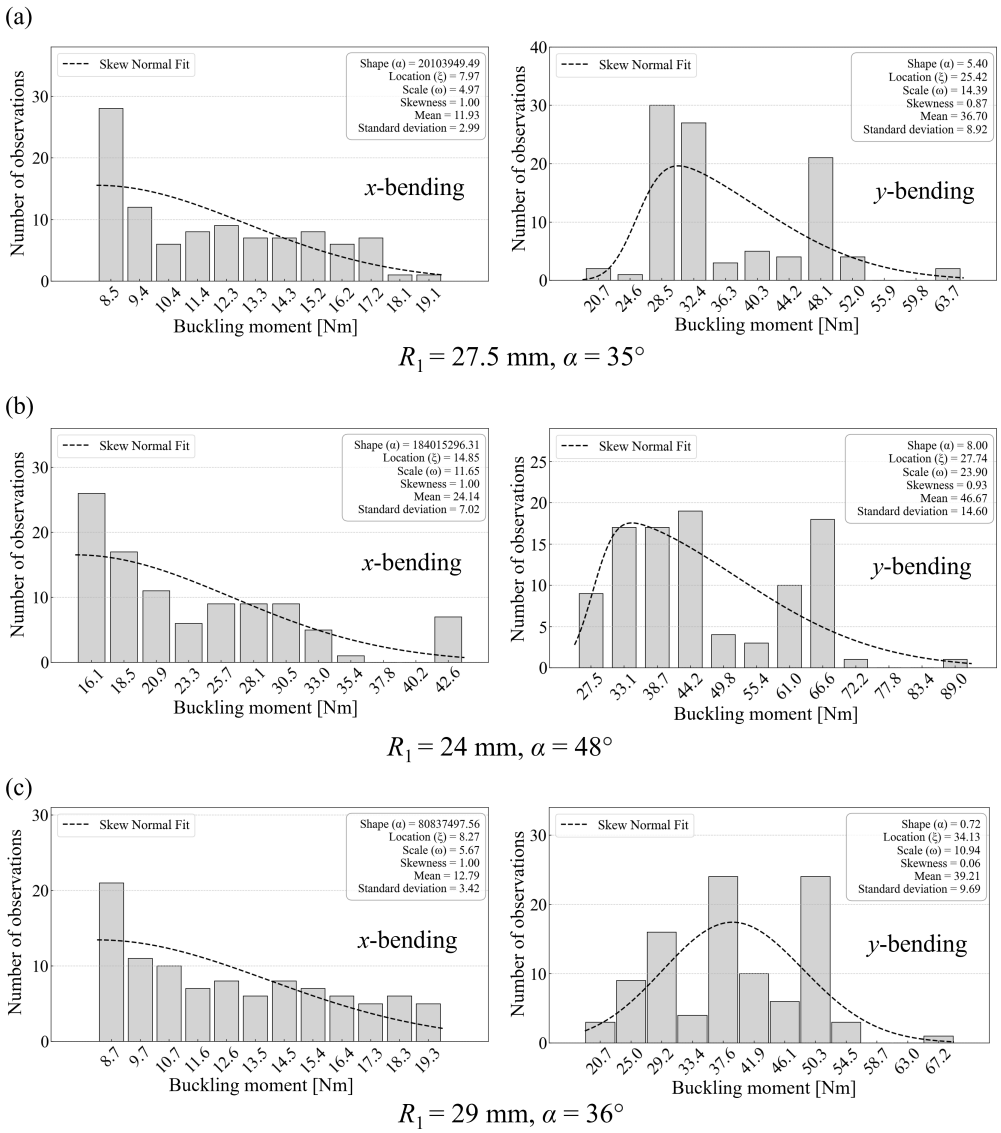


Figure B.1: Number of buckling moment observations for a dimple imperfection under different input geometries: (a) $R_1 = 27.5\,mm$, $\alpha = 35°$; (b) $R_1 = 24\,mm$, $\alpha = 48°$; (c) $R_1 = 29\,mm$, $\alpha = 36°$. In each subfigure, the left panel shows results for applying x-bending, and the right panel for applying y-bending.

References

[1] R. Ren, X. Ma, H. Yue, F. Yang, Y. Lu, Stiffness enhancement methods for thin-walled aircraft structures: A review, Thin-Walled Structures (2024) 111995.

[2] D. Mhadgut, A. Phoenix, J. Black, Data-driven rational approximation for composite boom deployment on a cubesat via vector-fitting, in: AIAA SCITECH 2024 Forum, 2024, p. 0410.

[3] A. Lalisani, M. Sadighi, T. Goudarzi, R. Alderliesten, R. Hedayati, Stiffened composite plates as equivalent structures for sandwich panels under low-velocity hail impact, Mechanics Based Design of Structures and Machines (2025) 1–28.

[4] M. Arya, N. Lee, S. Pellegrino, Ultralight structures for space solar power satellites, in: 3rd AIAA Spacecraft Structures Conference, 2016, p. 1950.

[5] F. Royer, J. W. Hutchinson, S. Pellegrino, Probing the stability of thin-shell space structures under bending, International Journal of Solids and Structures 257 (2022) 111806.

[6] F. Royer, S. Pellegrino, Experimentally probing the stability of thin-shell structures under pure bending, Philosophical Transactions of the Royal Society A 381 (2244) (2023) 20220024.

[7] S. M. Mojtabaei, J. Becque, R. Khandan, I. Hajirasouliha, Machine learning-based predictions of buckling behaviour of cold-formed steel structural elements, ce/papers 6 (3-4) (2023) 843–847.

[8] M. Hilburger, Developing the next generation shell buckling design factors and technologies, in: 53rd AIAA/ASME/ASCE/AHS/ASC structures, structural dynamics and materials conference 20th AIAA/ASME/AHS adaptive structures conference 14th AIAA, 2012, p. 1686.

[9] D. O. Brush, B. O. Almroth, J. Hutchinson, Buckling of bars, plates, and shells (1975).

[10] J. Hutchinson, W. Koiter, et al., Postbuckling theory, Appl. Mech. Rev 23 (12) (1970) 1353–1366.

[11] J. Singer, J. Arbocz, T. Weller, Buckling experiments: experimental methods in buckling of thin-walled structures, volume 2: shells, built-up structures, composites and additional topics, Vol. 2, John Wiley & Sons, 2002.

[12] T. Von Karman, H.-S. Tsien, The buckling of thin cylindrical shells under axial compression, Journal of the Aeronautical Sciences 8 (8) (1941) 303–312.

[13] W. T. Koiter, On the stability of elastic equilibrium, National Aeronautics and Space Administration, 1967.

[14] L. Donnell, C. Wan, Effect of imperfections on buckling of thin cylinders and columns under axial compression (1950).

[15] C. D. Babcock, The buckling of cylindrical shells with an initial imperfection under axial compression loading, Ph.D. thesis, California Institute of Technology (1962).

[16] V. I. Weingarten, P. Seide, J. P. Peterson, Buckling of thin-walled circular cylinders, Tech. rep. (1968).

[17] H. Abramovich, The vibration correlation technique–a reliable nondestructive method to predict buckling loads of thin walled structures, Thin-Walled Structures 159 (2021) 107308.

[18] D. Weisz-Patrault, P. Margerit, A. Constantinescu, Residual stresses in thin walled-structures manufactured by directed energy deposition: In-situ measurements, fast thermo-mechanical simulation and buckling, Additive Manufacturing 56 (2022) 102903.

[19] D. Bushnell, Buckling of shells-pitfall for designers, AIAA journal 19 (9) (1981) 1183–1226.

[20] G. W. Hunt, E. L. Neto, Localized buckling in long axially-loaded cylindrical shells, Journal of the Mechanics and Physics of Solids 39 (7) (1991) 881–894.

[21] J. Thompson, L. Virgin, Spatial chaos and localization phenomena in nonlinear elasticity, Physics Letters A 126 (8-9) (1988) 491–496.

[22] J. Horák, G. J. Lord, M. A. Peletier, Cylinder buckling: the mountain pass as an organizing center, SIAM Journal on Applied Mathematics 66 (5) (2006) 1793–1824.

[23] V. Tvergaard, A. Needleman, Buckling localization in a cylindrical panel under axial compression, International journal of solids and structures 37 (46-47) (2000) 6825–6842.

[24] R. Groh, A. Pirrera, On the role of localizations in buckling of axially compressed cylinders, Proceedings of the Royal Society A 475 (2224) (2019) 20190006.

[25] B. Audoly, J. W. Hutchinson, Localization in spherical shell buckling, Journal of the Mechanics and Physics of Solids 136 (2020) 103720.

[26] J. W. Hutchinson, J. M. T. Thompson, Nonlinear buckling behaviour of spherical shells: barriers and symmetry-breaking dimples, Philosophical Transactions of the Royal Society A: Mathematical, Physical and Engineering Sciences 375 (2093) (2017) 20160154.

[27] C. Cervi, L. Virgin, An experimental parametric study assessing the effect of a certain initial geometric imperfection on cylinder buckling, Aerospace Science and Technology 152 (2024) 109355.

[28] A. Abramian, E. Virot, E. Lozano, S. M. Rubinstein, T. M. Schneider, Nondestructive prediction of the buckling load of imperfect shells, Physical Review Letters 125 (22) (2020) 225504.

[29] N. L. Cuccia, K. Kumar Yadav, M. Serlin, E. Virot, S. Gerasimidis, S. M. Rubinstein, Hitting the mark: probing at the initiation site allows for accurate prediction of a thin shell's buckling load, Philosophical Transactions of the Royal Society A 381 (2244) (2023) 20220036.

[30] J. W. Hutchinson, J. M. T. Thompson, Imperfections and energy barriers in shell buckling, International Journal of Solids and Structures 148 (2018) 157–168.

[31] F. Derveni, F. Choquart, A. Abbasi, D. Yan, P. M. Reis, The most severe imperfection governs the buckling strength of pressurized multi-defect hemispherical shells, arXiv preprint arXiv:2410.08973 (2024).

[32] A. Lee, F. López Jiménez, J. Marthelot, J. W. Hutchinson, P. M. Reis, The geometric role of precisely engineered imperfections on the critical buckling load of spherical elastic shells, Journal of Applied Mechanics 83 (11) (2016) 111005.

[33] F. Derveni, A. Abbasi, P. M. Reis, Defect–defect interactions in the buckling of imperfect spherical shells, Journal of Applied Mechanics 92 (4) (2025).

[34] F. L. Jiménez, J. Marthelot, A. Lee, J. W. Hutchinson, P. M. Reis, Technical brief: knockdown factor for the buckling of spherical shells containing large-amplitude geometric defects, Journal of Applied Mechanics 84 (3) (2017) 034501.

[35] A. Abbasi, F. Derveni, P. M. Reis, Comparing the buckling strength of spherical shells with dimpled versus bumpy defects, Journal of Applied Mechanics 90 (6) (2023) 061008.

[36] D. Yan, M. Pezzulla, P. M. Reis, Buckling of pressurized spherical shells containing a through-thickness defect, Journal of the Mechanics and Physics of Solids 138 (2020) 103923.

[37] U. K. Ubamanyu, Z. Baizhikova, J.-L. Le, R. Ballarini, P. M. Reis, A numerical study on the buckling of near-perfect spherical shells, Journal of Applied Mechanics 92 (5) (2025) 051003.

[38] J. M. Fernandez, Advanced deployable shell-based composite booms for small satellite structural applications including solar sails, in: International Symposium on Solar Sailing 2017, no. NF1676L-25486, 2017.

[39] D. Crouch, Mars viking surface sampler subsystem, in: Proceedings of the 25th conference on remote systems technology, 1977, pp. 141–152.

[40] H. Armstrong, J. RR, Organic and metal matrix composites for spacecraft applications. (1978).

[41] A. J. Lee, J. M. Fernandez, Inducing bistability in collapsible tubular mast booms with thin-ply composite shells, Composite Structures 225 (2019) 111166.

[42] F. Palmeri, S. Laurenzi, A multi-objective optimization approach to design bistable collapsible tubular mast, Composite Structures 351 (2025) 118593.

[43] F. Palmeri, S. Laurenzi, Neural network-based surrogate modeling for buckling performance optimization of lightweight-composite collapsible tubular masts, Biomimetics 9 (8) (2024) 494.

[44] T. Duan, A. Anand, D. Y. Ding, K. K. Thai, S. Basu, A. Ng, A. Schuler, Ngboost: Natural gradient boosting for probabilistic prediction, in: International conference on machine learning, PMLR, 2020, pp. 2690–2700.

[45] R. Vieira, F. Virtuoso, E. Pereira, Buckling of thin-walled structures through a higher order beam model, Computers & Structures 180 (2017) 104–116.

[46] L. Huang, B. Li, Y. Wang, Computation analysis of buckling loads of thin-walled members with open sections, Mathematical Problems in Engineering 2016 (1) (2016) 8320469.

[47] J. W. Hutchinson, Buckling of spherical shells revisited, Proceedings of the Royal Society A: Mathematical, Physical and Engineering Sciences 472 (2195) (2016) 20160577.

[48] J. M. Fernandez, A. J. Lee, Bistable collapsible tubular mast booms, in: International Conference on Advanced Lightweight Structures and Reflector Antennas, no. NF1676L-30217, 2018.

[49] A. Fathi, S. Lalisani, F. Royer, Quantifying the effect of local imperfections on the buckling energy barrier of thin-shell structures, in: AIAA SCITECH 2025 Forum, 2025, p. 1197.

[50] F. Royer, S. Pellegrino, Experimentally probing the stability of thin-shell structures under pure bending, Philosophical Transactions of the Royal Society A: Mathematical, Physical and Engineering Sciences 381 (2244) (2023). doi:10.1098/rsta.2022.0024.

[51] M. T. Roudsari, M. Gordini, Random imperfection effect on reliability of space structures with different supports, Structural Engineering and Mechanics 55 (3) (2015) 461–472.

[52] I. M. Sobol', On the distribution of points in a cube and the approximate evaluation of integrals, Zhurnal Vychislitel'noi Matematiki i Matematicheskoi Fiziki 7 (4) (1967) 784–802.

[53] I. M. Sobol, Uniformly distributed sequences with an additional uniform property, USSR Computational mathematics and mathematical physics 16 (5) (1976) 236–242.

[54] T. W. Simpson, J. D. Poplinski, P. N. Koch, J. K. Allen, Metamodels for computer-based engineering design: survey and recommendations, Engineering with computers 17 (2001) 129–150.

[55] D. P. Murthy, M. Xie, R. Jiang, Weibull models, John Wiley & Sons, 2004.

[56] Z. Baizhikova, R. Ballarini, J.-L. Le, Uncovering the dual role of dimensionless radius in buckling of spherical shells with random geometric imperfections, Proceedings of the National Academy of Sciences 121 (16) (2024) e2322415121.

[57] J.-L. Le, Statistical scaling in localization-induced failures, Applied Mechanics Reviews 76 (6) (2024) 060801.

[58] A. Azzalini, A class of distributions which includes the normal ones, Scandinavian journal of statistics (1985) 171–178.

[59] A. Azzalini, The skew-normal and related families, Vol. 3, Cambridge University Press, 2013.

[60] C. Calladine, Understanding imperfection-sensitivity in the buckling of thin-walled shells, Thin-walled structures 23 (1-4) (1995) 215–235.

[61] P. Goldberg, C. Williams, C. Bishop, Regression with input-dependent noise: A gaussian process treatment, Advances in neural information processing systems 10 (1997).

[62] O. Ozbayram, A. Olivier, L. Graham-Brady, Heteroscedastic gaussian process regression for material structure–property relationship modeling, Computer Methods in Applied Mechanics and Engineering 431 (2024) 117326.

[63] T. Lee, J. S. Liu, Multi-response heteroscedastic gaussian process models and their inference, arXiv preprint arXiv:2308.15370 (2023).

[64] J. H. Friedman, Greedy function approximation: a gradient boosting machine, Annals of statistics (2001) 1189–1232.

[65] M. Bessa, S. Pellegrino, Design of ultra-thin shell structures in the stochastic post-buckling range using bayesian machine learning and optimization, International Journal of Solids and Structures 139 (2018) 174–188.

[66] T.-T. Wong, P.-Y. Yeh, Reliable accuracy estimates from k-fold cross validation, IEEE Transactions on Knowledge and Data Engineering 32 (8) (2019) 1586–1594.

[67] D. S. Soper, Greed is good: Rapid hyperparameter optimization and model selection using greedy k-fold cross validation, Electronics 10 (16) (2021) 1973.

[68] N. M. Al-Abdaly, S. R. Al-Taai, H. Imran, M. Ibrahim, Development of prediction model of steel fiber-reinforced concrete compressive strength using random forest algorithm combined with hyperparameter tuning and k-fold cross-validation, Eastern-European Journal of Enterprise Technologies 5 (7) (2021) 113.

[69] V. W. Lumumba, D. Kiprotich, N. Makena, M. Kavita, M. Mpaine, Comparative analysis of cross-validation techniques: Loocv, k-folds cross-validation, and repeated k-folds cross-validation in machine learning models, Am. J. Theor. Appl. Stat 13 (2024) 127–137.

[70] W. Zhang, J. Suhr, N. A. Koratkar, Observation of high buckling stability in carbon nanotube polymer composites, Advanced Materials 18 (4) (2006) 452–456.

[71] K. Deb, A. Pratap, S. Agarwal, T. Meyarivan, A fast and elitist multiobjective genetic algorithm: Nsga-ii, IEEE transactions on evolutionary computation 6 (2) (2002) 182–197.

[72] S. Chand, M. Wagner, Evolutionary many-objective optimization: A quick-start guide, Surveys in Operations Research and Management Science 20 (2) (2015) 35–42.

[73] M. Akbari, P. Asadi, M. Besharati Givi, G. Khodabandehlouie, Artificial neural network and optimization, Advances in friction-stir welding and processing 2 (2014) 543–599.

[74] S. Sharma, V. Kumar, A comprehensive review on multi-objective optimization techniques: Past, present and future, Archives of Computational Methods in Engineering 29 (7) (2022) 5605–5633.

[75] S. Brown, V. Sundara, S. Martynov, H. Mahgerefteh, Optimal valve spacing for next generation co2 pipelines, in: Computer Aided Chemical Engineering, Vol. 33, Elsevier, 2014, pp. 265–270.

[76] J. Blank, K. Deb, Pymoo: Multi-objective optimization in python, Ieee access 8 (2020) 89497–89509.

[77] H. Seada, K. Deb, U-nsga-iii: a unified evolutionary optimization procedure for single, multiple, and many objectives: proof-of-principle results, in: International conference on evolutionary multi-criterion optimization, Springer, 2015, pp. 34–49.

[78] N. Beume, B. Naujoks, M. Emmerich, Sms-emoa: Multiobjective selection based on dominated hypervolume, European Journal of Operational Research 181 (3) (2007) 1653–1669.

[79] N. Beume, C. M. Fonseca, M. Lopez-Ibanez, L. Paquete, J. Vahrenhold, On the complexity of computing the hypervolume indicator, IEEE Transactions on Evolutionary Computation 13 (5) (2009) 1075–1082.

[80] K. Shang, H. Ishibuchi, W. Chen, Y. Nan, W. Liao, Hypervolume-optimal μ-distributions on line/plane-based pareto fronts in three dimensions, IEEE Transactions on Evolutionary Computation 26 (2) (2021) 349–363.

[81] N. L. Cuccia, M. Serlin, K. K. Yadav, S. Lachmann, S. Gerasimidis, S. M. Rubinstein, A universal localized failure mechanism for real cylindrical shells, arXiv preprint arXiv:2412.01057 (2024).

[82] M. R. Rafique, Non-linear buckling analysis of thin-walled cylindrical shell having large openings, in: Pressure Vessels and Piping Conference, Vol. 88483, American Society of Mechanical Engineers, 2024, p. V002T03A068.

[83] L. E. de Castro Saiki, G. F. Gomes, Comparative analysis of modal, static, and buckling behaviors in thin-walled composite cylinders: A detailed study, Composite Structures 352 (2025) 118672.